OPTIMAL STRATEGIES FOR CONTINUOUS GRAVITATIONAL WAVE DETECTION IN PULSAR TIMING ARRAYS

Justin A. Ellis[1], Xavier Siemens[1], and Jolien D.E. Creighton[1]

Draft version April 20, 2012

ABSTRACT

Supermassive black hole binaries (SMBHBs) are expected to emit continuous gravitational waves in the pulsar timing array (PTA) frequency band (10^{-9}–10^{-7} Hz). The development of data analysis techniques aimed at efficient detection and characterization of these signals is critical to the gravitational wave detection effort. In this paper we leverage methods developed for LIGO continuous wave gravitational searches, and explore the use of the $\mathcal{F}$-statistic for such searches in pulsar timing data. Babak & Sesana 2012 have already used this approach in the context of PTAs to show that one can resolve multiple SMBHB sources in the sky. Our work improves on several aspects of prior continuous wave search methods developed for PTA data analysis. The algorithm is implemented fully in the time domain, which naturally deals with the irregular sampling typical of PTA data and avoids spectral leakage problems associated with frequency domain methods. We take into account the fitting of the timing model, and have generalized our approach to deal with both correlated and uncorrelated colored noise sources. We also develop an incoherent detection statistic that maximizes over all pulsar dependent contributions to the likelihood. To test the effectiveness and sensitivity of our detection statistics, we perform a number of monte-carlo simulations. We produce sensitivity curves for PTAs of various configurations, and outline an implementation of a fully functional data analysis pipeline. Finally, we present a derivation of the likelihood maximized over the gravitational wave phases at the pulsar locations, which results in a vast reduction of the search parameter space.

1. INTRODUCTION

In the next few years pulsar timing arrays (PTAs) are expected to detect gravitational waves (GWs) in the frequency range 10^{-9}–10^{-7} Hz. Potential sources of GWs in this frequency range include supermassive black hole binary systems (SMBHBs) (Sesana et al. 2008), cosmic (super)strings (Olmez et al. 2010), inflation (Starobinsky 1979), and a first order phase transition at the QCD scale (Caprini et al. 2010). The community has thus far mostly focused on stochastic backgrounds produced by these sources, but they can manifest themselves in different ways. Cosmic strings and SMBHBs (in highly eccentric orbits) can also produce GW bursts (Damour & Vilenkin 2001; Siemens et al. 2007; Leblond et al. 2009) in which the duration of the GW signal is much less than the observation time. Sufficiently nearby single SMBHBs may produce detectable continuous waves with periods on the order of years (Wyithe & Loeb 2003; Sesana et al. 2009; Sesana & Vecchio 2010). The concept of a PTA, an array of accurately timed millisecond pulsars, was first conceived of over two decades ago (Romani 1989; Foster & Backer 1990). Twenty years later three main PTAs are in full operation around the world: the North American Nanohertz Observatory for Gravitational waves (NANOGrav; Jenet et al. (2009)), the Parkes Pulsar Timing Array (PPTA; Manchester (2008)), and the European Pulsar Timing Array (EPTA; Janssen et al. (2008)). The three PTAs collaborate to form the International Pulsar Timing Array (IPTA; Hobbs et al. (2010)).

Prior to the establishment of PTAs, Jenet et al. (2004) used existing pulsar data to rule out the proposed SMBHB system 3C66B, a possible source of continuous GWs (the mass of the proposed system has since been been lowered significantly (Iguchi et al. 2010) so that it not likely to be detectable with current PTAs). In this work, the authors looked for the signature of a continuous GW in real pulsar data through the use of Lomb-Scargle periodograms and suggested a method for directed searches of known sources. Yardley et al. (2010) also relied on the Lomb-Scargle periodogram to determine the sensitivity of the PPTA to continuous GW sources as a function of GW frequency. van Haasteren & Levin (2010) developed a bayesian framework aimed at the detection of GW memory in PTAs; however, the authors mention that the methods presented could be used for continuous GW sources as well. Sesana & Vecchio (2010) use an Earth-term only signal model to perform a study of SMBHB parameters measurable with PTAs using a Fisher matrix approach. Corbin & Cornish (2010) have developed a Bayesian Markov Chain Monte-Carlo (MCMC) data analysis algorithm for parameter estimation of a SMBHB system in which the pulsar term is taken into account in the detection scheme, thereby increasing the SNR and improving the accuracy of the GW source location on the sky. Recently, Lee et al. (2011) have developed parameter estimation techniques based on vector Ziv-Zakai bounds incorporating the pulsar term and have placed limits on the minimum detectable amplitude of a continuous GW source. In this work, the authors also propose a method of combining timing parallax measurements with single-source GW detections to improve pulsar distance measurements.

In the context of searches for continuous gravitational waves from spinning neutron stars in LIGO, Jaranowski et al. (1998) developed the so-called $\mathcal{F}$-statistic, the logarithm of the likelihood ratio maximized over some of the signal parameters. Cutler & Schutz (2005) later generalized the $\mathcal{F}$-statistic to multi-detector networks. Very recently, Babak & Sesana (2012) have used the $\mathcal{F}$-statistic to show that in PTA data multiple SMBHB sources can be resolved in the sky. In this paper we build on this work, and improve on a number aspects of prior continuous wave search methods developed for PTA data analysis.

[1] Center for Gravitation and Cosmology, University of Wisconsin Milwaukee, Milwaukee WI, 53211

In Section 2 we review the signal model. In Section 3 we discuss the $\mathcal{F}$-statistic in the context of PTA data. Unlike LIGO implementations of the $\mathcal{F}$-statistic, our algorithm is implemented fully in the time domain. This naturally deals with the irregular sampling of PTA data and avoids the spectral leakage problems that arise when frequency domain methods are used on such data. We also account for the timing model: fitting out pulsar parameters removes signal power at low frequencies, at frequencies near 1 yr^{-1} and 2 yr^{-1} due to sky location, proper motion, and parallax fitting, and for pulsars in binaries, at frequencies near the binary orbital frequency. Our approach also naturally incorporates colored noise sources, both uncorrelated and correlated (for the case when the dominant noise source is a gravitational wave stochastic background). We also develop an incoherent detection statistic that maximizes over all pulsar dependent contributions to the likelihood. To test the effectiveness and sensitivity of our detection statistics, in Section 4 we perform a number of monte-carlo simulations. We produce sensitivity curves for PTAs of various configurations, and show that the performance of the incoherent statistic is comparable to the coherent $\mathcal{F}$-statistic. We also present an outline of the implementation of a continuous wave search pipeline. Finally, in Section 5 we summarize our results and conclude with a derivation of the likelihood maximized over the gravitational wave phases at the pulsar locations, which results in a vast reduction of the search parameter space. We leave the exploration of this new statistic for future work.

2. THE SIGNAL MODEL

In this section we will briefly review the form of the residuals induced by a non-spinning SMBHB in a circular orbit and introduce our notation. The GW is defined as a metric perturbation to flat space time defined as

$$h_{ab}(t,\hat{\Omega}) = e^+_{ab}(\hat{\Omega})h_+(t,\hat{\Omega}) + e^\times_{ab}(\hat{\Omega})h_\times(t,\hat{\Omega}), \quad (1)$$

where $\hat{\Omega}$ is the unit vector pointing from the GW source to the SSB, h_+, $h_\times$ and e^A_{ab} ($A = +, \times$) are the polarization amplitudes and polarization tensors, respectively. The polarization tensors can be converted to the Solar System Barycenter (SSB) by the following transformation. Following Wahlquist (1987) we write

$$e^+_{ab}(\hat{\Omega}) = \hat{m}_a\hat{m}_b - \hat{n}_a\hat{n}_b, \quad (2)$$

$$e^\times_{ab}(\hat{\Omega}) = \hat{m}_a\hat{n}_b + \hat{n}_a\hat{m}_b, \quad (3)$$

where

$$\hat{\Omega} = -(\sin\theta\cos\phi)\hat{x} - (\sin\theta\sin\phi)\hat{y} - (\cos\theta)\hat{z}, \quad (4)$$

$$\hat{m} = -(\sin\phi)\hat{x} + (\cos\phi)\hat{y}, \quad (5)$$

$$\hat{n} = -(\cos\theta\cos\phi)\hat{x} - (\cos\theta\sin\phi)\hat{y} + (\sin\theta)\hat{z}. \quad (6)$$

In this coordinate system, $\theta = \pi/2 - \delta$ and $\phi = \alpha$ are the polar and azimuthal angles of the source, respectively, where δ and α are declination and right ascension in usual celestial coordinates.

We will write our GW induced pulsar timing residuals in the following form:

$$s(t,\hat{\Omega}) = F^+(\hat{\Omega})\Delta s_+(t) + F^\times(\hat{\Omega})\Delta s_\times(t), \quad (7)$$

where

$$\Delta s_A(t) = s_A(t_p) - s_A(t_e), \quad (8)$$

and t_e and t_p are the times at which the GW passes the Earth and pulsar, respectively, and the index A labels polarizations. The functions $F^A(\hat{\Omega})$ are known as antenna pattern functions and are defined by

$$F^+(\hat{\Omega}) = \frac{1}{2}\frac{(\hat{m}\cdot\hat{p})^2 - (\hat{n}\cdot\hat{p})^2}{1 + \hat{\Omega}\cdot\hat{p}} \quad (9)$$

$$F^\times(\hat{\Omega}) = \frac{(\hat{m}\cdot\hat{p})(\hat{n}\cdot\hat{p})}{1 + \hat{\Omega}\cdot\hat{p}}, \quad (10)$$

where $\hat{p}$ is the unit vector pointing from the Earth to the pulsar. Also, from geometry we can write

$$t_p = t_e - L(1 + \hat{\Omega}\cdot\hat{p}). \quad (11)$$

Given these definitions, we can write the GW contributions to the timing residuals as (Wahlquist 1987; Corbin & Cornish 2010)

$$s_+(t) = \frac{\mathcal{M}^{5/3}}{D\omega(t)^{1/3}}\Big[-\sin[2(\Phi(t) - \Phi_0)](1 + \cos^2\iota)\cos 2\psi$$
$$- 2\cos[2(\Phi(t) - \Phi_0)]\cos\iota\sin 2\psi\Big] \quad (12)$$

$$s_\times(t) = \frac{\mathcal{M}^{5/3}}{D\omega(t)^{1/3}}\Big[-\sin[2(\Phi(t) - \Phi_0)](1 + \cos^2\iota)\sin 2\psi$$
$$+ 2\cos[2(\Phi(t) - \Phi_0)]\cos\iota\cos 2\psi\Big], \quad (13)$$

where

$$\Phi(t) = \frac{1}{32\mathcal{M}^{5/3}}\left(\omega_0^{-5/3} - \omega(t)^{-5/3}\right) \quad (14)$$

and

$$\omega(t) = \left(\omega_0^{-8/3} - \frac{256}{5}\mathcal{M}^{5/3}t\right)^{-3/8}. \quad (15)$$

For reasons that will become clear later, we write the residuals for pulsar α in the following form

$$r_\alpha(t,\hat{\Omega}) = s_\alpha(t,\hat{\Omega}) + n_\alpha(t)$$
$$= \sum_{i=1}^4 \left[a_i(\zeta,\iota,\Phi_0,\psi)A^i_\alpha(t,\theta,\phi,\omega_0)\right] \quad (16)$$
$$+ p_\alpha(t,\zeta,\iota,\Phi_0,\psi,\theta,\phi,\omega_0,L_\alpha) + n_\alpha(t),$$

where $\zeta = \mathcal{M}^{5/3}D^{-1}$, $n_\alpha(t)$ is the noise in each pulsar and

$$p_\alpha = F^+(\hat{\Omega})s_+(t_p) + F^\times(\hat{\Omega})s_\times(t_p). \quad (17)$$

Hereon we will refer to the summation term as the Earth term and p as the pulsar term. We write the combination of chirp mass and distance to the binary as one parameter because the two can not be disentangled unless there is a measurement of $\dot{f}$, which we do not consider here. It is customary to label the parameters $(\zeta,\iota,\Phi_0,\psi)$ and (θ,ϕ,ω_0) extrinsic and intrinsic parameters (Jaranowski et al. 1998), respectively. We then define the amplitudes and time dependent basis functions

$$a_1 = \zeta\left[(1 + \cos^2\iota)\cos\Phi_0\cos 2\psi + 2\cos\iota\sin\Phi_0\sin 2\psi\right]$$
$$a_2 = -\zeta\left[(1 + \cos^2\iota)\sin\Phi_0\cos 2\psi - 2\cos\iota\cos\Phi_0\sin 2\psi\right]$$
$$a_3 = \zeta\left[(1 + \cos^2\iota)\cos\Phi_0\sin 2\psi - 2\cos\iota\sin\Phi_0\cos 2\psi\right] \quad (18)$$
$$a_4 = -\zeta\left[(1 + \cos^2\iota)\sin\Phi_0\sin 2\psi + 2\cos\iota\cos\Phi_0\cos 2\psi\right]$$

and

$$A_\alpha^1 = F_\alpha^+(\hat{\Omega})\omega(t)^{-1/3}\sin(2\Phi(t))$$
$$A_\alpha^2 = F_\alpha^+(\hat{\Omega})\omega(t)^{-1/3}\cos(2\Phi(t))$$
$$A_\alpha^3 = F_\alpha^\times(\hat{\Omega})\omega(t)^{-1/3}\sin(2\Phi(t))$$
$$A_\alpha^4 = F_\alpha^\times(\hat{\Omega})\omega(t)^{-1/3}\cos(2\Phi(t)).$$
(19)

Throughout this work we assume that the source is slowly evolving (i.e. the phase is independent of the chirp mass) and $\omega(t) \approx \omega_0$ and $\Phi(t) \approx \omega_0 t$.

3. THE LIKELIHOOD FUNCTION AND THE $\mathcal{F}$-STATISTIC

Here we will introduce our formalism and derive the likelihood and $\mathcal{F}$-statistic (the likelihood maximized over extrinsic parameters) for PTAs. We will also discuss the statistics of the $\mathcal{F}$-statistic in the presence and absence of a signal and show that we obtain the expected behavior for PTA data.

3.1. Likelihood

For a pulsar timing array with M pulsars we define the likelihood function of the noise as multivariate gaussian

$$p(\mathbf{n}) = \frac{1}{\sqrt{2\pi\Sigma_n}}\exp\left(-\frac{1}{2}\mathbf{n}^T\Sigma_n^{-1}\mathbf{n}\right),$$
(20)

where

$$\mathbf{n} = \begin{bmatrix} n_1 \\ n_2 \\ \vdots \\ n_M \end{bmatrix}$$
(21)

is the vector of the noise time-series for all pulsars,

$$\Sigma_n = \begin{bmatrix} \Sigma_{n,1} & S_{12} & \dots & S_{1M} \\ S_{21} & \Sigma_{n,2} & \dots & S_{2M} \\ \vdots & \vdots & \ddots & \vdots \\ S_{1M} & S_{2M} & \dots & \Sigma_{n,M} \end{bmatrix}$$
(22)

is the multivariate covariance matrix, and

$$\Sigma_{n,i} = \langle \mathbf{n}_i \mathbf{n}_i \rangle$$
(23)
$$S_{ij} = \langle \mathbf{n}_i \mathbf{n}_j \rangle|_{i\neq j}$$
(24)

are the auto-covariance and cross-covariance matrices of the pulsar noise, respectively. It is important to note that in the case of uncorrelated noise, the off-diagonal cross covariance matrices vanish. In order to time pulsars, a timing model is fitted out of the pulsar times-of-arrival (TOAs) via a weighted least squares fitting routine (Hobbs et al. 2006). This procedure can be expressed via a data-independent linear operator $\mathbf{R}$ (see Demorest et al. 2012 for details) so that

$$\tilde{\mathbf{n}} = \mathbf{R}\mathbf{n},$$
(25)

where

$$\mathbf{R} = \begin{bmatrix} R_1 \\ R_2 \\ \vdots \\ R_M \end{bmatrix}$$
(26)

is a vector of matrices R_i, the fitting operators for each pulsar, and $\tilde{\mathbf{n}}$ is the post-fit noise. We can see the effect of this
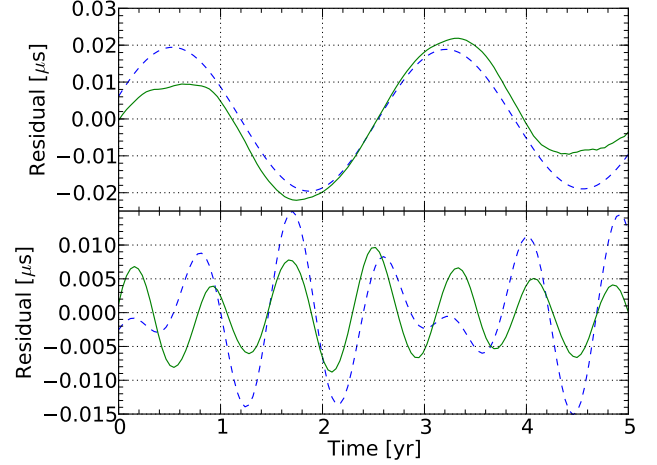

Figure 1. SMBHB waveforms in two different regimes. Each plot shows the waveform before (dotted blue) and after fitting (solid green) for a full timing model including spin-down, astrometric and binary parameters. Top Panel: The Earth and pulsar terms at the same frequency. Bottom Panel: The Earth term and pulsar term at different frequencies.

fitting procedure on the waveforms in Fig. 1 where the waveform is changed, quite significantly, from its pre-fit form. It is straightforward to show that the likelihood for the fitted $\tilde{\mathbf{n}}$ is

$$p(\tilde{\mathbf{n}}) = \frac{1}{\sqrt{2\pi\Sigma_{\tilde{n}}}}\exp\left(-\frac{1}{2}\tilde{\mathbf{n}}^T\Sigma_{\tilde{n}}^{-1}\tilde{\mathbf{n}}\right),$$
(27)

where

$$\Sigma_{\tilde{n}} = \langle \tilde{\mathbf{n}}\tilde{\mathbf{n}}^T \rangle = \mathbf{R}\langle \mathbf{n}\mathbf{n}^T \rangle \mathbf{R}^T.$$
(28)

The fitted residuals can therefore be written as

$$\mathbf{r} = \mathbf{R}(\mathbf{s}+\mathbf{n}) = \tilde{\mathbf{s}}+\tilde{\mathbf{n}},$$
(29)

where

$$\mathbf{r} = \begin{bmatrix} r_1 \\ r_2 \\ \vdots \\ r_M \end{bmatrix}, \qquad \mathbf{s} = \begin{bmatrix} s_1 \\ s_2 \\ \vdots \\ s_M \end{bmatrix}$$
(30)

are the residual data and signal template for each pulsar, respectively. We can therefore write the likelihood of the data $\mathbf{r}$ given some signal template $\mathbf{s}$

$$p(\mathbf{r}|\mathbf{s}) = \frac{1}{\sqrt{2\pi\Sigma_{\tilde{n}}}}\exp\left(-\frac{1}{2}(\mathbf{r}-\tilde{\mathbf{s}})^T\Sigma_{\tilde{n}}^{-1}(\mathbf{r}-\tilde{\mathbf{s}})\right).$$
(31)

We define the inner product for two time vectors $\mathbf{x}$ and $\mathbf{y}$ using the noise covariance matrix Σ_n as

$$\left(\mathbf{x}|\mathbf{y}\right) = \mathbf{x}^T\Sigma_{\tilde{n}}^{-1}\mathbf{y}.$$
(32)

In this notation we can write the log of the likelihood ratio as

$$\ln\Lambda = \ln\frac{p(\mathbf{r}|\mathbf{s})}{p(\mathbf{r}|0)} = (\mathbf{r}|\tilde{\mathbf{s}}) - \frac{1}{2}(\tilde{\mathbf{s}}|\tilde{\mathbf{s}}).$$
(33)

It is worth pointing out that finding the inverse of $\Sigma_{\tilde{n}}$ is computationally intensive. Aside from it being a very large matrix, the fitting procedure results in loss of degrees of freedom in the data which makes $\Sigma_{\tilde{n}}$ singular. Inverting this matrix therefore requires singular value decomposition.

In most realistic scenarios we can assume that the off-diagonal cross-covariance matrices are small and expand the

inverse of Eq. 22 in a Neumann series (see Eq. 72 of Anholm et al. 2009 for details). In the simulations shown later in the paper we will assume that any correlated noise is much less than the uncorrelated part, thus we treat $\Sigma_{\tilde{n}}$ as a block diagonal matrix of the auto-covariance matrices for each pulsar.

3.2. *The Earth-term $\mathcal{F}$-statistic*

We now analytically maximize over the extrinsic parameters $(\zeta, \iota, \Phi_0, \psi)$ in the signal model. A very similar calculation was first done by Jaranowski et al. (1998) in the context of LIGO, subsequently by Cornish & Porter (2007) in the context of LISA, and very recently by Babak & Sesana (2012) in the context of pulsar timing. For clarity, here we review this calculation in the notation introduced above. For this calculation we treat the pulsar term as a noise source and write our signal template in the form

$$\mathbf{s}(t, \hat{\Omega}) = \sum_{i=1}^{4} a_i(\zeta, \iota, \Phi_0, \psi) \mathbf{A}^i(t, \theta, \phi, \omega_0), \quad (34)$$

where

$$\mathbf{A}^i = \begin{bmatrix} A_1^i \\ A_2^i \\ \vdots \\ A_M^i \end{bmatrix}. \quad (35)$$

Later we will explain the circumstances under which it is safe to drop the pulsar term. We can now write the log-likelihood as

$$\ln \Lambda = a_i(\mathbf{r}|\mathbf{A}^i) - \frac{1}{2}(\mathbf{A}^i|\mathbf{A}^j)a_i a_j = a_i \mathbf{N}^i - \frac{1}{2}\mathbf{M}^{ij}a_i a_j. \quad (36)$$

Maximizing the log-likelihood ratio over the four amplitudes a_i gives

$$\frac{\partial \ln \Lambda}{\partial a_k} = 0 = \mathbf{N}^i \delta_i^k - \frac{1}{2}\mathbf{M}^{ij}a_j \delta_i^k - \frac{1}{2}\mathbf{M}^{ij}a_i \delta_j^k$$
$$= \mathbf{N}^k - \mathbf{M}^{ik}a_i, \quad (37)$$

yielding the maximum likelihood estimators for the four amplitudes

$$a_i = \mathbf{M}_{ij}\mathbf{N}^j, \quad (38)$$

where $\mathbf{M}_{ij} = (\mathbf{M}^{ij})^{-1}$. Substituting these back into the likelihood results in the $\mathcal{F}_e$-statistic

$$2\mathcal{F}_e = \mathbf{N}^i \mathbf{M}_{ij}\mathbf{N}^j. \quad (39)$$

The statistics of $2\mathcal{F}_e$ are a χ^2 with 4 degrees of freedom and a non-centrality parameter $\bar{\rho}^2$. It is straightforward to show that the expectation value is

$$\langle 2\mathcal{F}_e \rangle = 4 + \bar{\rho}^2$$
$$= 4 + (\tilde{\mathbf{s}}|\tilde{\mathbf{s}}) + 2(\tilde{\mathbf{p}}|\tilde{\mathbf{s}}) + (\tilde{\mathbf{p}}|\mathbf{A}^i)\mathbf{M}_{ij}(\tilde{\mathbf{p}}|\mathbf{A}^j), \quad (40)$$

where $\mathbf{p}$ is the functional form of the pulsar term and the second two terms in $\bar{\rho}^2$ are due to the fact that we have only included the Earth term in our templates $\mathbf{s}$. In Figs. 2(c) and 2(d) we can see that the probability distribution functions of $2\mathcal{F}_e$ follow the expected distributions in the absence and presence of a signal. While only the intrinsic parameters are formally searched over, it is also possible to get estimates of the

maximized extrinsic parameters by constructing the following quantities (Cornish & Porter 2007):

$$A_+ = \sqrt{(a_1+a_4)^2 + (a_2-a_3)^2}$$
$$+ \sqrt{(a_1-a_4)^2 + (a_2+a_3)^2}, \quad (41)$$

$$A_\times = \sqrt{(a_1+a_4)^2 + (a_2-a_3)^2}$$
$$- \sqrt{(a_1-a_4)^2 + (a_2+a_3)^2} \quad (42)$$

and

$$A = A_+ + \sqrt{A_+^2 + A_\times^2}. \quad (43)$$

It is then possible to recover the maximized parameters

$$\iota = \cos^{-1}\left(\frac{-A_\times}{A}\right), \quad (44)$$

$$\psi = \frac{1}{2}\tan^{-1}\left(\frac{A_+ a_4 - A_\times A_1}{A_\times a_3 + A_+ a_2}\right), \quad (45)$$

$$\Phi_0 = -\tan^{-1}\left(\frac{-(A_\times a_1 - A_+ a_4)}{(A_+ a_3 + A_\times a_2)}\right), \quad (46)$$

$$\zeta = \frac{Ac}{4}, \quad (47)$$

where $c = sgn(\sin 2\psi)$. It is interesting to examine the case of one pulsar. In this case, Eq. 37 has no solution because the matrix $\mathbf{M}$ is singular. The reason for this is that it is incorrect to write the residuals in the form of Eq. 16 with four degrees of freedom. For one pulsar, the signal has only *two* degrees of freedom: an amplitude and a phase, or equivalently, two unknown amplitudes, thereby making the maximization over *four* independent amplitudes an ill-posed problem. Thus, at least two pulsars are needed to solve Eq. 37. It should be noted that it is straightforward to generalize this statistic to N GW sources, we will simply have $4N$ independent amplitudes instead of just 4 (see Babak & Sesana 2012 for more details). However, for simplicity in this work we will deal with just one GW source.

3.2.1. *Justification for dropping the pulsar term*

There are two cases in which the pulsar term is truly negligible to the $\mathcal{F}_e$-statistic and can be dropped from the analysis with no change in the statistics.

The first is the astrophysically likely scenario in which the evolution of the GW frequency is such that the Earth and pulsar terms are in different frequency bins (see e.g. Figure 2 of Sesana & Vecchio 2010). At the frequency of the Earth term the signal will build up coherently. The pulsar term signals, even if they all happen to be at the same frequency, will not because they have different phases that depend on the the pulsar distances. This effect is illustrated in Fig. 3(a) where the reference χ^2 distribution has 4 degrees of freedom and non-centrality parameter $(\tilde{\mathbf{s}}|\tilde{\mathbf{s}})$.

The second case is the less astrophysically likely scenario in which the Earth and pulsar term lie in the same frequency bin. In this case, there is still a phase difference between the Earth and pulsar terms. We expect that for a large number of pulsars the pulsar term signals will cancel because they all have different phases. We can see from Fig. 2(d) that for a moderate number of pulsars ($M = 20$ in this case) the pulsar phases do not completely cancel and our measured values of the $\mathcal{F}_e$-statistic are higher than expected with just the earth
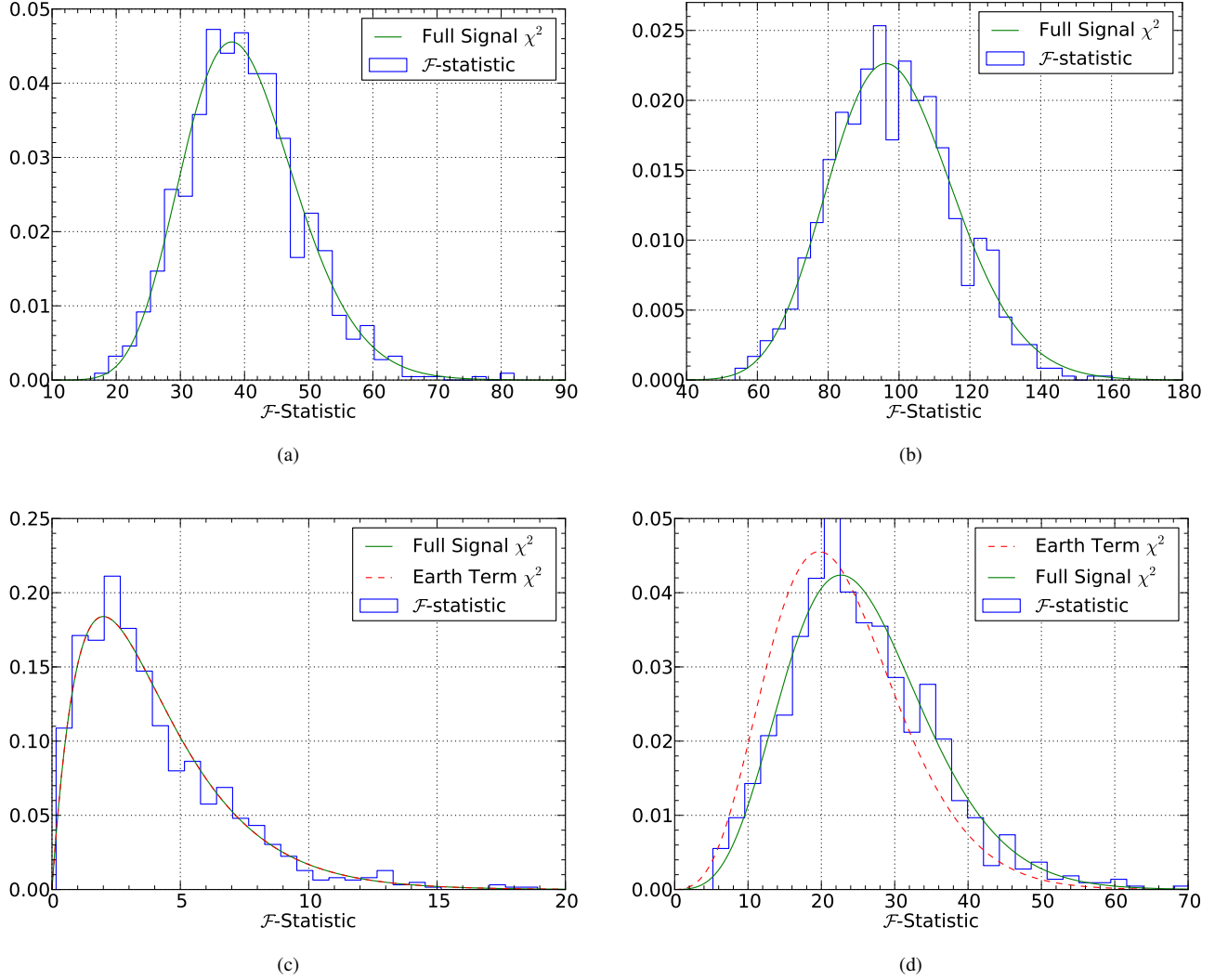
(a)

(b)

(c)

(d)

Figure 2. Histograms and expected probability distribution functions of $2\mathcal{F}_p$ and $2\mathcal{F}_e$ in the absence and presence of a signal for 20 pulsars. Each simulation was done with the search parameters fixed and 1000 realizations of white gaussian noise. (a): distribution of $2\mathcal{F}_p$ in the absence of a signal. (b): distribution of $2\mathcal{F}_p$ in the presence of a signal with non-centrality parameter ρ^2. (c): distribution of $2\mathcal{F}_e$ in the absence of a signal. (d): distribution of $2\mathcal{F}_e$ in the presence of a signal. The dashed (red) and solid (green) curves have the same meaning as in Fig. 3.

term because the last two terms of Eq. 40 do not sum to zero. However, in the case of large M ($M \gtrsim 50$) the pulsar term contributions sum approximately to zero, and again we have a χ^2 distribution with 4 degrees of freedom and non-centrality parameter $(\tilde{\mathbf{s}}|\tilde{\mathbf{s}})$.

If we happen to detect a signal that falls into the intermediate category mentioned above where $M < 50$ and some or all of the pulsar terms are in the same frequency bin as the Earth term, then this will create a bias in the recovered sky location but not in our ability to confidently detect the signal (see Fig.1 of Ellis et al. (2012a)). This is because our detection criterion is the false alarm probability. As will be discussed in detail in Section 3.4, the false alarm probability only depends on the probability distribution function when the signal is *absent*, and we can see from Fig. 2(a) that $2\mathcal{F}_e$ follows the expected distribution, because it is independent of the signal properties.

3.3. *The incoherent $\mathcal{F}$-statistic*

It is indeed possible to include the pulsar term in our analysis if we operate in the low frequency (or low chirp mass) regime where the frequency evolution of the source is slow enough that the frequency at the Earth and the pulsar are essentially the same so that the signal is a sum of two sinusoids of different phases: the pulsar term and the Earth term. To understand this more quantitatively, consider the Taylor series expansion of the orbital frequency of Eq. 15 evaluated at the pulsar time

$$
\begin{aligned}
\omega(t_p) &= \omega_0 \left(1 - \frac{256}{5} \mathcal{M}^{5/3} \omega_0^{8/3} t_p \right)^{-3/8} \\
&\approx \omega_0 \left(1 + \frac{96}{5} \mathcal{M}^{5/3} \omega_0^{8/3} \left[t_e - L(1 + \hat{\Omega} \cdot \hat{p}) \right] \right).
\end{aligned}
\tag{48}
$$

From this, we can see that $\omega(t_p) \approx \omega_0$ when

$$
\omega_0 \ll \left(\frac{5}{96} \mathcal{M}^{-5/3} \left| \left(T - L(1 + \hat{\Omega} \cdot \hat{p}) \right) \right| \right)^{3/8}, \tag{49}
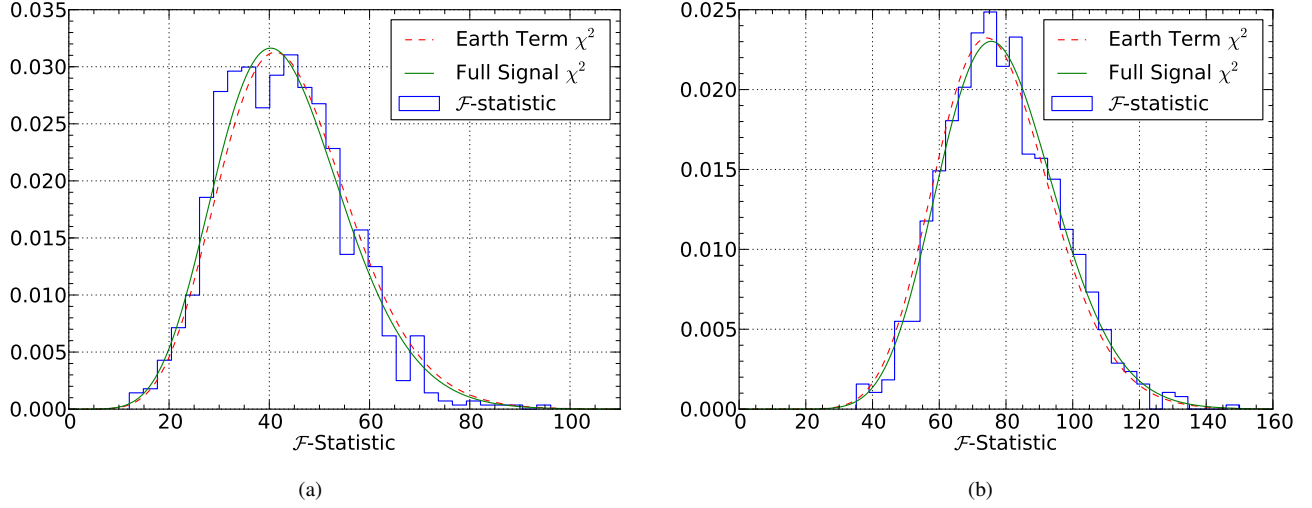$$

(a)

(b)

Figure 3. Probability distribution functions for $2\mathcal{F}_e$ in the limits that the pulsar term is negligible. (a): probability distribution function in the limit that all pulsar terms lie outside the Earth term frequency bin. (b): probability distribution function in the limit of large M for overlapping Earth and pulsar term frequencies. The dashed (red) curve is a χ^2 distribution with a non-centrality parameter assuming that only the Earth term is present in the data. The solid (green) curve is a χ^2 distribution with non-centrality parameter $\bar{\rho}^2$ that takes both the Earth and pulsar term into account.

where T is the total observation time. If we consider only one intrinsic parameter, ω_0, then the template for pulsar α is

$$s_\alpha(t,\hat{\Omega}) = \sum_{i=1}^{2} b_{i\alpha}(\zeta,\iota,\psi,\Phi_0,\phi_\alpha,\theta,\phi)B_\alpha^i(t,\omega_0), \quad (50)$$

where

$$\phi_\alpha = \omega L_\alpha(1+\hat{\Omega}\cdot\hat{p}_\alpha)+\Phi_0 \quad (51)$$

is the pulsar dependent phase. We can now write the pulsar dependent amplitudes and basis functions as

$$b_{1\alpha} = \zeta\Bigg[(1+\cos^2\iota)(F_\alpha^+\cos 2\psi+F_\alpha^\times\sin 2\psi)(\cos\Phi_0-\cos\phi_\alpha)$$
$$+2\cos\iota(F_\alpha^+\sin 2\psi-F_\alpha^\times\cos 2\psi)(\sin\Phi_0-\sin\phi_\alpha)\Bigg]$$
$$(52)$$

$$b_{2\alpha} = -\zeta\Bigg[(1+\cos^2\iota)(F_\alpha^+\cos 2\psi+F_\alpha^\times\sin 2\psi)(\sin\Phi_0-\sin\phi_\alpha)$$
$$-2\cos\iota(F_\alpha^+\sin 2\psi-F_\alpha^\times\cos 2\psi)(\cos\Phi_0-\cos\phi_\alpha)\Bigg]$$
$$(53)$$

and

$$B_\alpha^1(t) = \frac{1}{\omega_0^{1/3}}\sin(2\omega_0 t) \quad (54)$$

$$B_\alpha^2(t) = \frac{1}{\omega_0^{1/3}}\cos(2\omega_0 t), \quad (55)$$

where, again, ω_0 is the angular orbital frequency of the SMBHB. The log-likelihood ratio is

$$\ln\Lambda = \sum_{\alpha=1}^{M}\left[b_{i\alpha}(r_\alpha|B_\alpha^i)-\frac{1}{2}(B_\alpha^i|B_\alpha^j)b_{i\alpha}b_{j\alpha}\right]$$
$$= \sum_{\alpha=1}^{M}\left[b_{i\alpha}P_\alpha^i-\frac{1}{2}Q_\alpha^{ij}b_{i\alpha}b_{j\alpha}\right]. \quad (56)$$

Maximizing the likelihood ratio over the $2M$ amplitude parameters $b_{i\alpha}(\zeta,\iota,\psi,\Phi_0,\phi_\alpha,\theta,\phi)$ gives

$$\frac{\partial\ln\Lambda}{\partial b_{k\beta}} = 0 = \sum_{\alpha=1}^{M}\Bigg[P_\alpha^i\delta_i^k\delta_{\alpha\beta}-\frac{1}{2}Q_\alpha^{ij}b_{i\alpha}\delta_j^k\delta_{\alpha\beta}$$
$$-\frac{1}{2}Q_\alpha^{ij}b_{j\alpha}\delta_i^k\delta_{\alpha\beta}\Bigg] = P_\beta^k-Q_\beta^{ik}b_{i\beta} \quad (57)$$

which yields the solution for the maximum likelihood estimators of the $2M$ amplitudes

$$b_{i\beta} = Q_{ik}^\beta P_\beta^k. \quad (58)$$

Putting the amplitude estimators back into the likelihood ratio we obtain the $\mathcal{F}_p$-statistic

$$2\mathcal{F}_p = \sum_{\alpha=1}^{M}P_\alpha^i Q_{ij}^\alpha P_\alpha^j. \quad (59)$$

It is straightforward to then show that $2\mathcal{F}_p$ follows a χ^2 distribution with $2M$ degrees of freedom and non-centrality parameter $\hat{\rho}^2$ and that

$$\langle 2\mathcal{F}_p\rangle = 2M+\rho^2$$
$$= 2M+(\tilde{\mathbf{s}}|\tilde{\mathbf{s}}) \quad (60)$$

where $\rho^2 = (\tilde{\mathbf{s}}|\tilde{\mathbf{s}})$ is the optimal signal-to-noise ratio (see Fig. 2). Note that this is an *incoherent* detection statistic since it involves sum of the squares of the data, whereas the Earth-term $\mathcal{F}_e$-statistic is *coherent* since it involves the square of the sum of the data.

It is worth pointing out that for the case of white gaussian noise, the $\mathcal{F}_p$-statistic is the time domain equivalent to the weighted power spectral summing technique studied in Ellis et al. (2012a). For colored gaussian noise the statistic is the time domain equivalent to a weighted power spectral summing technique with frequency dependent weights. Another feature of this detection statistic is that it does not only apply to the low-frequency limit. If we work in the high frequency

regime where the Earth and the pulsar terms are in different frequency bins, we can drop the pulsar term and arrive at the exact same maximized likelihood function. In this case the pulsar dependence of the amplitudes $b_{i\alpha}$ comes from the antenna pattern functions the not the pulsar phase. However, many of the justifications for dropping the pulsar term mentioned in the previous section do not apply in this case since the statistic is incoherent. We find that this detection statistic will often pick out the pulsar term frequency over the Earth term frequency because the residuals of Eq. 16 scale like $\omega(t)^{-1/3}$ and the pulsar term will always be at an equal or lower frequency than the Earth term frequency due to the geometrical delay in Eq. 11. For this system of equations we have $2M$ equations and $6 + M$ unknowns, so if we have 6 or more pulsars we can solve for the all the parameters $(\zeta, \iota, \psi, \Phi_0, \theta, \phi)$ along with the pulsar phases ϕ_α.

3.4. *False alarm probability and detection statistics*

Here we review the false alarm and detection probability distribution functions both when the intrinsic parameters are known and unknown. Our discussion follows closely that of Jaranowski et al. (1998) and Jaranowski & Królak (2005). In the case of known extrinsic parameters, we have shown in Sections 3.2 and 3.3 that the statistics $2\mathcal{F}$ and $2\mathcal{F}_p$ follow χ^2 distributions with 4 and $4M$ degrees of freedom, respectively, when the signal is absent. It was also shown that the aforementioned statistics follow a non-central χ^2 with non-centrality parameters $\bar{\rho}$ and ρ, respectively, when the signal is present.

Therefore, the probability distribution functions p_0 and p_1 when the intrinsic parameters are known and when the signal is absent and present, respectively, are

$$p_0(\mathcal{F}) = \frac{\mathcal{F}^{n/2-1}}{(n/2-1)!} \exp(-\mathcal{F}) \qquad (61)$$

$$p_1(\mathcal{F}, \kappa) = \frac{(2\mathcal{F})^{(n/2-1)/2}}{\kappa^{n/2-1}} I_{n/2-1}\left(\kappa\sqrt{2\mathcal{F}}\right)$$
$$\times \exp\left(-\mathcal{F} - \frac{1}{2}\kappa^2\right), \qquad (62)$$

where n is the number of degrees of freedom, $I_{n/2-1}$ is the modified Bessel function of the first kind and order $n/2 - 1$, and κ is ρ for $\mathcal{F}_p$ and $\bar{\rho}$ for $\mathcal{F}_e$. The false alarm probability P_F is defined as the probability that $\mathcal{F}$ exceeds a given threshold $\mathcal{F}_0$ when no signal is present. In this case, we have

$$P_F(\mathcal{F}_0) = \int_{\mathcal{F}_0}^{\infty} p_0(\mathcal{F})d\mathcal{F} = \exp(-\mathcal{F}_0) \sum_{k=0}^{n/2-1} \frac{\mathcal{F}_0^k}{k!}. \qquad (63)$$

The probability of detection P_D is the probability that $\mathcal{F}$ exceeds the threshold $\mathcal{F}_0$ when the signal-to-noise ratio is κ:

$$P_D(\mathcal{F}_0, \kappa) = \int_{\mathcal{F}_0}^{\infty} p_1(\mathcal{F}, \kappa)d\mathcal{F}, \qquad (64)$$

however; we do not deal with the detection probability in this work. Our detection criterion is based on the false alarm probability.

We now turn to the more realistic problem of calculating the false alarm probability when the intrinsic parameters are not known. A detailed derivation and description is given in Jaranowski & Królak (2000), here we will simply review the result. The probability P_F^T that $\mathcal{F}$ exceeds $\mathcal{F}_0$ in one or more cells is given by

$$P_F^T(\mathcal{F}_0) = 1 - [1 - P_F(\mathcal{F}_0)]^{N_c}, \qquad (65)$$

where N_c is the number of independent cells in parameter space. The number of independent cells can be calculated via geometrical methods described in Jaranowski & Królak (2000) and references therein.

Here we will make the following approximations. For our $\mathcal{F}_p$ statistic we will set N_p to be equal to the number of independent frequency bins defined by the Nyquist frequency. For our $\mathcal{F}_e$ statistic, we will set N_c to be equal to the number of templates used in the search. In general the number of independent templates and the number of independent cells will be quite different. However, since we only have a three dimensional parameter space and use a nested sampling algorithm to conduct the search (thereby reducing the number of templates in low likelihood regions of parameter space), setting the number of templates equal to the number of independent cells is a reasonable assumption.

4. PIPELINE, SENSITIVITIES, AND IMPLEMENTATION

In this section we will test the $\mathcal{F}_e$ and $\mathcal{F}_p$ statistics on realistic simulated data sets. First, we will outline our detection pipeline, then we will briefly describe our simulated data sets and test the ability to confidently detect the signal and recover the injected intrinsic parameters. Finally, we perform monte-carlo simulations to produce sensitivity curves for PTAs of various configurations and sensitivities.

4.1. *Detection Pipeline*

The only inputs to our detection pipeline are the ephemeris file (typically called a "par" file) and TOA file (typically called a "tim" file) for each pulsar. The steps in the pipeline are as follows:

1. Use the standard pulsar timing package TEMPO2 (Hobbs et al. 2006) to form the residuals for each pulsar.

2. Use TEMPO2 plugin to output the design matrix for each pulsar (see Chapter 15 of Press et al. 1992 for more details). Then construct **R** from the design matrices following Demorest (2007).

3. Use a maximum likelihood eigenvalue decomposition method described in Ellis et al. (2012b) to make an estimate of $\Sigma_{\tilde{n}}$. Note that the cross terms in Eq. 22 are expected to be small, so we will ignore them for this work.

4. Follow the methods described in Secs. 3.2 and 3.3 to construct the detection statistics and search the relevant parameter space. If using the $\mathcal{F}_p$-statistic we simply grid up the frequency space for the search. If using the $\mathcal{F}_e$-statistic we use the nested sampling package, Multi-Nest (Feroz et al. 2009) to search the three dimensional parameter space.

5. Output the maximum value of the detection statistic and number of templates used and compute the relevant false alarm probability using Eq. 65. Here we set our false alarm probability threshold to 10^{-4}. If the false alarm probability corresponding to our maximum value of $\mathcal{F}$ is greater than 10^{-4} then we claim a detection.

6. Use the maximum likelihood estimators to find the extrinsic parameters (using Eqs. 44–47), and construct the posterior probability distribution to find the intrinsic parameters by sampling the maximized likelihood (Eq. 39). As mentioned above, when using the $\mathcal{F}_p$ statistic, one could use numerical techniques to obtain estimates of the extrinsic parameters.

7. Use the maximum likelihood values of the intrinsic and extrinsic parameters to construct Gaussian prior distributions and carry out parameter estimation on the the full 7 dimensional search space, again using MultiNest, to get better estimates of SMBHB parameters.

In this paper we will only conduct steps 1–5 and leave steps 6 and 7 for future work. Although this work uses simulated datasets, nothing in this detection pipeline makes any assumptions about the spacing of the data, or the color of the noise.

In the absence of a detection we would like to set upper limits on the strain amplitude as a function of GW frequency. This can be accomplished as follows

1. Run the detection pipeline and determine the value of the $\mathcal{F}$-statistic.

2. For each frequency, choose the value of ζ corresponding to a specific strain amplitude. Then inject a SMBHB signal with randomly drawn binary orientation parameters ($\cos\iota, \psi, \Phi_0$).

3. Run the detection pipeline again on this injected data and measure the value of the $\mathcal{F}$-statistic.

4. Keep the value of ζ fixed and perform a given number of injections with different binary orientation parameters (1000, for example) and determine the fraction of $\mathcal{F}$-statistic values that is larger than the value measured in the original data.

5. Repeat steps 2–4 until the strain amplitude is such that 95% of the injections give a value of the $\mathcal{F}$-statistic that is larger than the original value.

6. Record this value and repeat steps 2–5 at each frequency.

4.2. *Simulated data sets*

For this work we use a simulated pulsar timing array with sky locations drawn from uniform distributions in $\cos\theta$ and ϕ. All pulsars are assumed to have a distance of 1 kpc and a white noise rms of 100 ns with equal error bars. The timespan of the observations for all pulsars is 5 years with evenly spaced bimonthly TOA measurements. Each set of residuals has been created by fitting a full timing model including spin-down, astrometric, and binary parameters (see Edwards et al. 2006 for details). As a check in some simulations an uncorrelated red noise process with a power law spectrum $P(f) = Af^{-\gamma}$ is included in the residuals, which has no effect on our results. While these simulated data sets do not include uneven sampling or extra fitting procedures like jumps or time varying DM variations, they do capture the essence of real timing residuals in the quadratic fitting of the spin-down parameters and the yearly and half yearly sinusoidal trends due to the sky location, proper motion and parallax fitting. Very uneven sampling is likely to reduce our sensitivity at higher frequencies and a detailed study of this problem will be presented in future work.

4.3. *Implementation of the detection statistics*

Here we will test our detection statistics on mock data sets with injected SMBHB GW signals in the presence of white and red gaussian noise. We will focus primarily on the $\mathcal{F}_e$-statistic since, as we will show, it is a more robust detection statistic. Then, we will implement a procedure to produce an upper limit on the GW strain amplitude as a function of frequency for a simulated NANOGrav (Demorest et al. 2012) array and plausible SKA arrays.

Fig. 4 shows the posterior probability distributions of the intrinsic search parameters for simulated SMBHB signals in the presence of 100 ns white noise (Fig. 4(a)) and uncorrelated red noise with amplitude $A = 4.22 \times 10^{-33}$ s$^{-2.09}$ and $\gamma = 4.1$. The two cases do have different realizations of the white noise, however, we can see that the $\mathcal{F}_e$-statistic does a very good job of determining the frequency and sky location of the source. In general, the $\mathcal{F}_e$-statistic is more robust than the $\mathcal{F}_p$ statistic because it produces estimates of the sky location as well as the frequency, which is very important when looking for electromagnetic counterparts.

It is possible to produce a sensitivity curve by a method that is similar to what we use to set upper limits. In this case we use simulated data with a given level of noise and no signal present. We follow the method presented in Sec. 4.1 except we now look for strain amplitude that gives a false alarm probability that is higher than our threshold (10^{-4} in our case) in 95% of realizations for each frequency. For clarity, we define the strain amplitude as

$$h = 2\frac{\mathcal{M}^{5/3}(\pi f_{\mathrm{gw}})^{2/3}}{D}, \qquad (66)$$

where $f_{\mathrm{gw}} = \omega_0/\pi$. This amplitude comes from the overall scaling factor that results in differentiating Eq. 12 and 13 with respect to time. For simplicity and speed we have simplified this method for our sensitivity plots. Instead of performing a search at each frequency, we simply evaluate the $\mathcal{F}_e$ and $\mathcal{F}_p$ statistics at the values of the injected parameters. The purpose of these sensitivity plots is to illustrate the overall features of the different detection statistics and to give order of magnitude estimates of expected sensitivity for real data.

We have produced various sensitivity curves for both the $\mathcal{F}_e$ and $\mathcal{F}_p$ statistics in Fig. 5. The three scenarios that we look at are a 17 pulsar simulated NANOGrav array in which we use the real sky location and timing models of the NANOGrav pulsars, and simulated PTAs with 25 and 100 pulsars at random sky locations. The loss in sensitivity at GW frequencies of $1\,\mathrm{yr}^{-1}$ and $2\,\mathrm{yr}^{-1}$ are due to the fitting of the pulsar's sky location and proper motion, and parallax, respectively. It is important to note that the sensitivity curves for the $\mathcal{F}_e$ and $\mathcal{F}_p$ statistics in the 17 and 25 pulsar cases, respectively, are very similar. Conversely, for the case of 100 pulsars the $\mathcal{F}_e$ statistic is more sensitive by a factor of ~ 2 for almost all frequencies. This is due to the different scaling relations of the statistics vs. the number of pulsars ($\mathcal{F}_e \propto \sqrt{M}$ while $\mathcal{F}_p \propto M^{1/4}$). However, the plot shows that the $\mathcal{F}_p$-statistic is more sensitive at lower frequencies and the $\mathcal{F}_e$-statistic is more sensitive at higher frequencies. There are two effects that contribute to this. The first is a result of our simulation and stems from the fact that we assume that for a given frequency, the maximum value of the $\mathcal{F}_e$-statistic is at the injected sky location. However, for low frequencies where the Earth and pulsar term are in the same frequency bin this assumption breaks down as
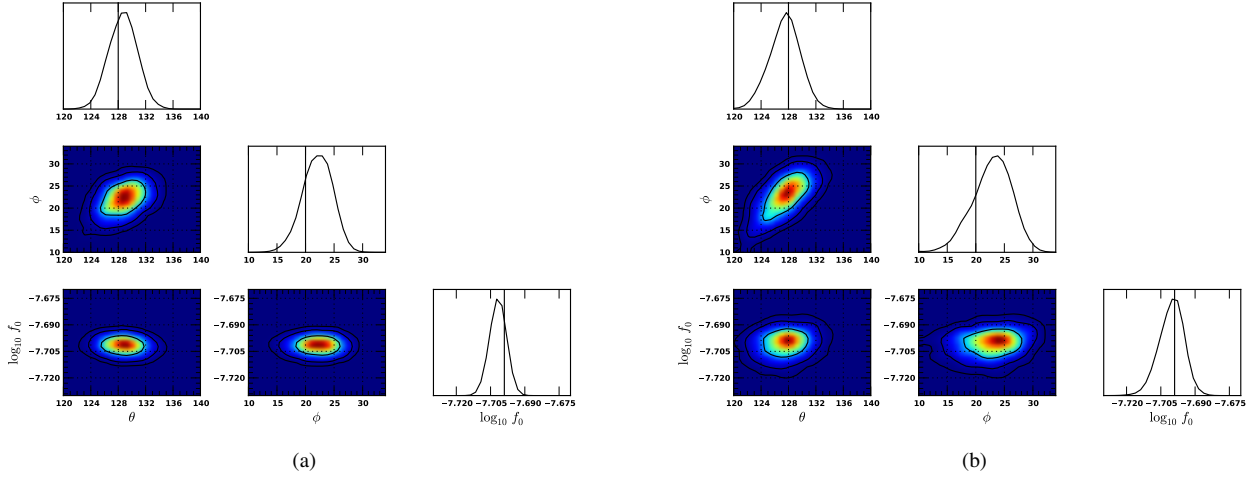
(a)   (b)

Figure 4. Posterior probability distribution functions for sky location and orbital frequency for a network SNR=14 injection with and without red noise. Here we have used a PTA with 25 pulsars. The vertical lines indicated the injected parameters and the contours are the one, two and three sigma contours. (a): 100 ns white noise. (b): 100 ns white noise and uncorrelated red noise with amplitude $A = 4.22 \times 10^{-33}$ s$^{-2.09}$ and $\gamma = 4.1$. We see that the sky location and orbital frequency have all been recovered at the one-sigma level in both cases.

the sky location will be biased (see e.g. Ellis et al. 2012a). The second effect is one inherent to our detection statistics themselves. As discussed in Sec. 3.3, the $\mathcal{F}_p$-statistic has different meanings in the low and high frequency regimes. In the low frequency regime, it effectively contains the entire signal (Earth and pulsar terms), and in the high frequency regime it only contains the Earth term piece since the pulsar terms are out of that frequency bin. This distinction results in a different scaling relation for the ratio of $\mathcal{F}_e/\mathcal{F}_p$. In the low frequency case the $\mathcal{F}_e$-statistic scales coherently but it only has approximately *half* of the signal, whereas, the $\mathcal{F}_p$-statistic scales incoherently but has the *full* signal. Therefore, the ratio scales as $M^{1/4}/2$, thus the incoherent method will do better

for $M \leq 16$. Conversely, in the high frequency regime, both statistics contain only *half* of the signal and the ratio scales as $M^{1/4}$. Therefore, the coherent statistic will do about a factor of 2 better than the incoherent method for $M \geq 16$.

5. SUMMARY AND OUTLOOK

In this work we have adapted the standard $\mathcal{F}$-statistic (Jaranowski et al. 1998) to act as a detection statistic for continuous wave searches in realistic PTA data. We have also developed an incoherent detection statistic that maximizes over all pulsar contributions to the likelihood. Both of these detection statistics are implemented in the time domain to avoid spectral leakage problems associated with Fourier domain methods applied to irregularly sampled data. These methods take the pulsar timing model fitting into account and have been generalized to account for both correlated and uncorrelated colored noise. Most of our analysis relies on dropping the pulsar term from our signal model as it will not add coherently. We have justified the use of this approximation in most astrophysically likely scenarios. It was shown that both of the detection statistics follow well known χ^2 distributions in the presence and absence of GW signals and therefore have well defined false-alarm probabilities. We have shown that the $\mathcal{F}_e$ statistic can not only confidently detect a GW signal but can also determine the sky location and frequency of the source to relatively high accuracy in the presence of white and colored gaussian noise. A realistic implementation of a fully functional continuous GW pipeline starting from basic pulsar timing data and methods for computing upper limits on the strain amplitude were outlined in detail. Finally, we have used simulated data sets of various PTA configurations to produce sensitivity curves for our $\mathcal{F}$-statistics. From these sensitivity curves, we have shown that the sensitivity of the $\mathcal{F}_e$ and $\mathcal{F}_p$ statistics are very similar for $M \leq 25$ pulsars and that the $\mathcal{F}_e$ statistic becomes more sensitive for $M > 25$ and for higher frequencies.

As was shown in Ellis et al. (2012a), explicitly searching over the pulsar distances or somewhat equivalently, the GW phases at the pulsar locations (in the low frequency regime), is
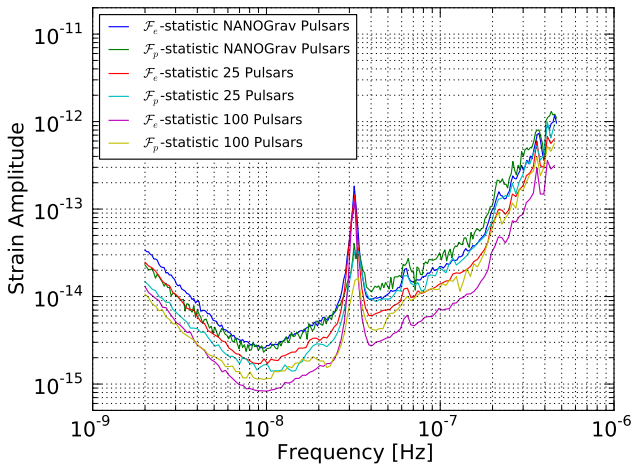

Figure 5. Sensitivity curves for the $\mathcal{F}_e$ and $\mathcal{F}_p$ statistics for different PTA configurations (all pulsars have 100 ns residuals). The blue and green lines are the sensitivity curves for the $\mathcal{F}_e$ and $\mathcal{F}_p$ statistics, respectively, for a simulated NANOGrav PTA. The red and cyan lines are the sensitivity curves for the $\mathcal{F}_e$ and $\mathcal{F}_p$ statistics, respectively, for a simulated PTA with 25 pulsars. The magenta and yellow lines are the sensitivity curves for the $\mathcal{F}_e$ and $\mathcal{F}_p$ statistics, respectively, for a simulated PTA with 100 pulsars.

computationally prohibitive for $M \gtrsim 5$. A statistic that could maximize over these GW phases would greatly reduce the parameter space of the search, while still preserving the SNR of the full signal. The implementation of such an algorithm will be the subject of future work. However, we will give the derivation here. From Eq. 16, in the low-frequency limit we can write the signal in the following form

$$s_\alpha(t) = \sum_{i=0}^{M} \left[(\cos \Phi_\alpha - 1)\delta_{ij} + \sin \Phi_\alpha \varepsilon_{ij} \right] a^j A^i, \quad (67)$$

where $\Phi_\alpha = \omega L_\alpha(1 + \hat{\Omega} \cdot \hat{p}_\alpha)$, $a^i = a_i$ and A^i are defined in Eqs. 18 and 19, respectively, and the matix

$$\varepsilon = \begin{bmatrix} 0 & -1 & 0 & 0 \\ 1 & 0 & 0 & 0 \\ 0 & 0 & 0 & 1 \\ 0 & 0 & 1 & 0 \end{bmatrix}. \quad (68)$$

After some algebra, the log-likelihood ratio of Eq. 33 can be written as

$$\ln \Lambda = \sum_{\alpha=1}^{M} \left[b(\cos^2 \Phi_\alpha - \sin^2 \Phi_\alpha) + c \cos \Phi_\alpha \right.$$
$$\left. + d \sin \Phi_\alpha + f \sin \Phi_\alpha \cos \Phi_\alpha \right], \quad (69)$$

with

$$b = -\frac{1}{2} M_\alpha^{ij} a_i a_j \quad (70)$$

$$c = N_\alpha^i a_i + M_\alpha^{ij} a_i a_j \quad (71)$$

$$d = N_\alpha^i \varepsilon_{ij} a^j \quad (72)$$

$$f = -M_\alpha^{ij} \varepsilon_{\ell j} a_i a^\ell \quad (73)$$

where M_α and N_α are defined by the following relations

$$M_\alpha^{ij} = (A_\alpha^i | A_\alpha^j) \quad (74)$$

$$N_\alpha^i = (r_\alpha | A_\alpha^i). \quad (75)$$

Maximizing the log-likelihood with respect to the pulsar phases Φ_β, we obtain

$$\frac{\partial \ln \Lambda}{\partial \Phi_\beta} = f(\cos^2 \Phi_\beta - \sin^2 \Phi_\beta) + 2b \cos \Phi_\beta \sin \Phi_\beta$$
$$- c \sin \Phi_\beta + d \cos \Phi_\beta = 0. \quad (76)$$

Setting $x = \cos \Phi_\beta$, this expression reduces to a quartic equation of the form

$$0 = (4f^2 + 16b^2)x^4 + (4fd + 8cb)x^3$$
$$+ (c^2 - 4f^2 - 16b^2)x^2 + (-2fd - 8cb)x \quad (77)$$
$$+ f^2 - c^2$$

which is guaranteed to have at least one unique solution. This maximization results in a monumental reduction in the parameter space that needs to be searched. It takes on the order of $\sim 10^{2M}$ templates just to cover the pulsar phases (Ellis et al. 2012a). In practice, we could construct the various quantities M_α, N_α, $\mathbf{a}$, b, c, d, and f, solve Eq. 77 numerically to find the maximum likelihood estimators for all the pulsar phases. Substituting these solutions back into our likelihood Eq. 69 still leaves us with the problem of searching over a 7 dimensional parameter space (since the amplitudes $\mathbf{a}$ depend on 4

parameters $(\zeta, \iota, \Phi_0, \psi)$ and the basis functions $\mathbf{A}$ depend on 3 parameters (θ, ϕ, ω_0)). We note, however, that this can be easily handled with a Markov chain Monte-Carlo (MCMC) or nested sampling algorithm.

Looking to the future, the pipeline outlined in this paper will be used to analyze real pulsar timing residuals and, in the absence of a detection, construct upper limits on the strain amplitude as a function of frequency. We will also further develop and test our likelihood maximized over the GW phase at the pulsar on both simulated and real data. We will also begin to generalize the methods discussed in the this paper to deal with eccentric signal models.

REFERENCES

Anholm, M., Ballmer, S., Creighton, J. D. E., Price, L. R., & Siemens, X. 2009, Phys. Rev. D, 79, 084030
Babak, S., & Sesana, A. 2012, Phys. Rev. D, 85, 044034
Caprini, C., Durrer, R., & Siemens, X. 2010, Phys. Rev. D, D82, 063511
Corbin, V., & Cornish, N. J. 2010, arXiv:1008.1782
Cornish, N. J., & Porter, E. K. 2007, Classical and Quantum Gravity, 24, 5729
Cutler, C., & Schutz, B. F. 2005, Phys. Rev. D, 72, 063006
Damour, T., & Vilenkin, A. 2001, Phys. Rev. D, 64, 064008
Demorest, P. B. 2007, PhD thesis, University of California, Berkeley
Demorest, P. B., et al. 2012, arXiv:1201.6641
Edwards, R. T., Hobbs, G. B., & Manchester, R. N. 2006, MNRAS, 372, 1549
Ellis, J. A., Jenet, F. A., & McLaughlin, M. A. 2012a, arXiv:1202.0808
Ellis, J. A., et al. 2012b, in preparation
Feroz, F., Hobson, M. P., & Bridges, M. 2009, MNRAS, 398, 1601
Foster, R. S., & Backer, D. C. 1990, ApJ, 361, 300
Hobbs, G., et al. 2010, Classical and Quantum Gravity, 27, 084013
Hobbs, G. B., Edwards, R. T., & Manchester, R. N. 2006, MNRAS, 369, 655
Iguchi, S., Okuda, T., & Sudou, H. 2010, ApJL, 724, L166
Janssen, G. H., Stappers, B. W., Kramer, M., Purver, M., Jessner, A., & Cognard, I. 2008, in American Institute of Physics Conference Series, Vol. 983, 40 Years of Pulsars: Millisecond Pulsars, Magnetars and More, ed. C. Bassa, Z. Wang, A. Cumming, & V. M. Kaspi, 633–635
Jaranowski, P., & Królak, A. 2000, Phys. Rev. D, 61, 062001
—. 2005, Living Reviews in Relativity, 8, 3
Jaranowski, P., Królak, A., & Schutz, B. F. 1998, Phys. Rev. D, 58, 063001
Jenet, F., et al. 2009, arXiv:0909.1058
Jenet, F. A., Lommen, A., Larson, S. L., & Wen, L. 2004, ApJ, 606, 799
Leblond, L., Shlaer, B., & Siemens, X. 2009, Phys. Rev. D, 79, 123519
Lee, K. J., Wex, N., Kramer, M., Stappers, B. W., Bassa, C. G., Janssen, G. H., Karuppusamy, R., & Smits, R. 2011, MNRAS, 414, 3251
Manchester, R. N. 2008, in American Institute of Physics Conference Series, Vol. 983, 40 Years of Pulsars: Millisecond Pulsars, Magnetars and More, ed. C. Bassa, Z. Wang, A. Cumming, & V. M. Kaspi, 584–592
Olmez, S., Mandic, V., & Siemens, X. 2010, Phys.Rev., D81, 104028
Press, W. H., Teukolsky, S. A., Vetterling, W. T., & Flannery, B. P. 1992, Numerical recipes in C (2nd ed.): the art of scientific computing (New York, NY, USA: Cambridge University Press)
Romani, R. W. 1989, in Timing Neutron Stars, ed. H. Ögelman & E. P. J. van den Heuvel, 113–+
Sesana, A., & Vecchio, A. 2010, Phys. Rev. D, 81, 104008
Sesana, A., Vecchio, A., & Colacino, C. N. 2008, MNRAS, 390, 192
Sesana, A., Vecchio, A., & Volonteri, M. 2009, MNRAS, 394, 2255
Siemens, X., Mandic, V., & Creighton, J. 2007, Physical Review Letters, 98, 111101

Starobinsky, A. A. 1979, JETP Lett., 30, 682
van Haasteren, R., & Levin, Y. 2010, MNRAS, 401, 2372
Wahlquist, H. 1987, General Relativity and Gravitation, 19, 1101

Wyithe, J. S. B., & Loeb, A. 2003, ApJ, 590, 691
Yardley, D. R. B., et al. 2010, MNRAS, 407, 669